Research Article Vol. 8, No. 8 / August 2021 / Optica 1065

optica

Polarization-resolved second-harmonic generation imaging through a multimode fiber

Angel Cifuentes,[1,5] Tomáš Pikálek,[1] Petra Ondráčková,[1] Rodrigo Amezcua-Correa,[2] José Enrique Antonio-Lopez,[2] Tomáš Čižmár,[1,3,4] and Johanna Trägårdh[1,*]

[1]Institute of Scientific Instruments of the CAS, v. v. i., Královopolská 147, 612 64 Brno, Czech Republic
[2]CREOL, The College of Optics and Photonics, University of Central Florida, 4304 Scorpius St., 32816-2700 Orlando, Florida 32816, USA
[3]Leibniz Institute of Photonic Technology, Albert-Einstein-Straße 9, 07745 Jena, Germany
[4]Institute of Applied Optics, Friedrich Schiller University Jena, Fröbelstieg 1, 07743 Jena, Germany
[5]e-mail: cifuentes@isibrno.cz
*Corresponding author: e-mail: johanna@isibrno.cz

Received 28 April 2021; revised 1 July 2021; accepted 1 July 2021 (Doc. ID 430295); published 2 August 2021

Multimode fiber-based endoscopes have recently emerged as a tool for minimally invasive endoscopy in tissue, at depths well beyond the reach of multiphoton imaging. Here, we demonstrate label-free second-harmonic generation (SHG) microscopy through such a fiber endoscope. We simultaneously fully control the excitation polarization state and the spatial distribution of the light at the fiber tip, and we use this to implement polarization-resolved SHG imaging, which allows imaging and identification of structural proteins such as collagen and myosin. We image mouse tail tendon and heart tissue, employing the endoscope at depths up to 1 mm, demonstrating that we can differentiate these structural proteins. This method has the potential for enabling instant and *in situ* diagnosis of tumors and fibrotic conditions in sensitive tissue with minimal damage.

https://doi.org/10.1364/OPTICA.430295

1. INTRODUCTION

Current medical diagnosis of conditions such as cancer and fibrotic diseases, which manifest as changes in tissue structure, is largely based on performing a biopsy and subsequent histopathology off-site. A minimally invasive technique, which would allow analogous diagnostics instantly and *in situ*, would dramatically accelerate decision-making and reduce the need for repeat surgery. Hence, substantial efforts have been made to develop advanced optical imaging methods for this purpose, sometimes referred to as "optical biopsies" [1]. These methods rely on a variety of label-free optical imaging modalities, often used in combination, such as coherent anti-Stokes Raman spectroscopy (CARS) [2,3], two-photon fluorescence and second-harmonic generation (SHG) imaging [4–8]. These imaging methods are sensitive to the underlying tissue structure and composition that indicate the disease condition.

Since noninvasive approaches to light microscopy are hindered by the scattering effects of biological tissue, they fail to simultaneously offer sufficient resolution and penetration depth. Consequently, lens-based endoscopes emerged as powerful candidates for performing optical biopsies at depth [9,10]. However, these devices have footprints that may substantially impact the normal functioning of tissue. Recently, advances in wavefront shaping technologies, holographic control of light, and research into light propagation in complex media [11,12] have enabled the use of thin (∼100 μm) multimode optical fibers (MMFs) as laser scanning microendoscopes [13–18]. Such endoscopes are rapidly progressing into useful research tools, even for routine and high resolution *in vivo* brain imaging in animal models [15,16].

In this paper, we demonstrate second-harmonic generation imaging (SHGIM) [6] through a minimally invasive MMF-based endoscope with 125 μm diameter. SHGIM allows label-free imaging of, e.g., collagen, which is particularly relevant for diagnosing fibrotic diseases as well as for tumor diagnosis, where reorganization of the collagen-rich extracellular matrix is an indication of a pathology. The technique has shown promise in the study of multiple pathologies, e.g., liver and cardiac fibrosis [7,19].

The method relies on SHG in noncentrosymmetric structures, such as those found in endogenous structural proteins, e.g., myosin, microtubulin, and collagen. When these proteins interact with high-intensity laser pulses, a photon at half the excitation wavelength is generated and can be easily separated and detected, similar to fluorescence. SHG has been successfully demonstrated on fibrillar structures [20], such as striated muscle [21], and microtubules in mossy fibers in the brain [22] and connective tissue [23].

A particularly promising variation of SHGIM is polarization-resolved SHGIM [24,25], which relies on a variable polarization state of the excitation light to probe the second-order nonlinear susceptibility tensor, $\chi^{(2)}$ [26,27]. $\chi^{(2)}$ depends on the sample composition, chirality, and structural organization, e.g., local fibril orientation, and thus the polarization response allows us to probe these properties. Crucially, this method requires control

of the output polarization of the endoscope. Since MMFs do not maintain the polarization of light, the implementation is more complicated than in standard microscopy, where an electro-optic modulator (EOM) at the microscope input suffices. Here, we demonstrate a simple scheme for simultaneous spatial and polarization control in MMFs. We then use this scheme to implement linear polarization-resolved SHGIM through an MMF. The technique is demonstrated by imaging and characterizing collagen and myosin structures from a mouse tail and within the myocardial walls of a mouse heart, employing the endoscope at up to 1 mm depth.

Various methods for polarization control in random media have been demonstrated [28–30], also with some imaging applications [28]. Although these approaches work well for random media, it is not straightforward to implement those techniques directly in an MMF, and the technique we present here is more suitable for MMFs. The main obstacle with the methods in [28–31] is the requirement of strong mode coupling, which is not necessarily present in MMFs Furthermore, the polarization recovery in the method reported in [28] requires performing the calibration using a source with a bandwidth substantially larger than the bandwidth of the medium [28]. For a high bandwidth graded index (GRIN) fiber, the required source bandwidth would be several tens of nanometers, which is far more than the bandwidth of a standard 100 fs laser appropriate for bioimaging. Polarization control resulting in a focused spot with a single linear polarization in MMFs has been demonstrated [32], but generation of an arbitrary in-plane polarization state was not demonstrated, nor was it used for polarization-sensitive imaging. We also note that polarization control, but without spatial control (that is a static, but highly polarized speckle pattern, and no imaging) at the end of an optical fiber has been demonstrated through control of the spatial degree of freedom at the input [31]. This method also requires strong mode coupling. In that experiment, the mode coupling was artificially introduced by adding stresses to a 2 m long MMF. Such a fiber would not have a bandwidth suitable for nonlinear imaging using femtosecond pulses [33]. In contrast, here we obtain both spatial and polarization control at the fiber output (with no requirements on the degree of mode coupling) as suitable for imaging.

Furthermore, our method is not limited to linear polarization, but any in-plane polarization state can be created, e.g., left-handed and right-handed circular (LHC and RHC). This allows measurements of the SHG circular dichroism (CD), a quantity tied to the chirality of the sample and sensitive to the out-of-plane tilt [34]. Normalized SHG CD has shown potential for the study of pathologies such as pulmonary fibrosis [35] and ovarian cancer [36], and since it only requires two images to be acquired, it is faster than linear polarization-resolved SHGIM.

In the ultrathin endoscopes used here, detection of coherently generated signals can become problematic. Signals such as SHG and CARS are emitted mainly in the forward direction, and detection relies on backscattering from the tissue. Because of the small aperture of the detector, the detection efficiency is low [17]. Nevertheless, we demonstrate that the detection efficiency in our endoscope is sufficient for imaging. This problem does not arise for the detection of SHG through standard, larger diameter, microendoscopes, where SHGIM, although not polarization-resolved SHGIM, has been demonstrated [9,10,37,38].

Finally, in addition to standalone use as a diagnostic tool, SHG could also be used as a component of multimodal imaging [9,10]. Together with two-photon fluorescence and CARS imaging, which are methods that have already been demonstrated for MMF endoscopes [17,18], this would provide a minimally invasive approach to optical biopsies.

2. MATERIALS AND METHODS

We performed polarization-resolved SHGIM through a multimode GRIN fiber using a femtosecond laser emitting at 1040 nm as the excitation source. For MMF-based techniques, the imaging is preceded by a calibration step (described briefly below), taking about 5 min, in which the light transport through the fiber probe is characterized. Using this information, focal points can be created by coupling an appropriately shaped wavefront into the fiber. Each focal position corresponds to a specific pattern on the spatial light modulator (SLM) and by displaying a sequence of such patterns, the focus is scanned across a plane 15 μm from the output facet of the MMF, mimicking a laser scanning microscope.

A Experimental Setup

Figure 1 shows a simplified schematic of the experimental setup where a femtosecond laser (Chameleon Discovery, Coherent) emitting at 1040 nm was used as the excitation source. The beam was expanded to cover an active area of 720 pixels × 720 pixels of a Meadowlark HSP1920-1064-HSP8 liquid crystal-on-silicon phase-only SLM, operating in an off-axis configuration. The calibration module placed at the distal end of the fiber was removed during endoscopic imaging and was only required to characterize the light transport through the MMF.

The details of the setup and calibration procedure have been described in [33], and the details of the control of the input polarization, necessary when using GRIN fibers, which do not maintain the polarization of the propagating light, are described in [17]. In short, by displaying a hologram obtained from the complex addition of three blazed gratings, the SLM was used to split the laser beam into a reference beam and two beams that are coupled into the MMF. The polarization of one of the beams was rotated by 90° using a half-wave plate (HWP), and the beams were then combined on a polarizing beam splitter. This allowed us to control the two orthogonal polarization states required for full spatial and polarization control at the fiber output. During imaging, a

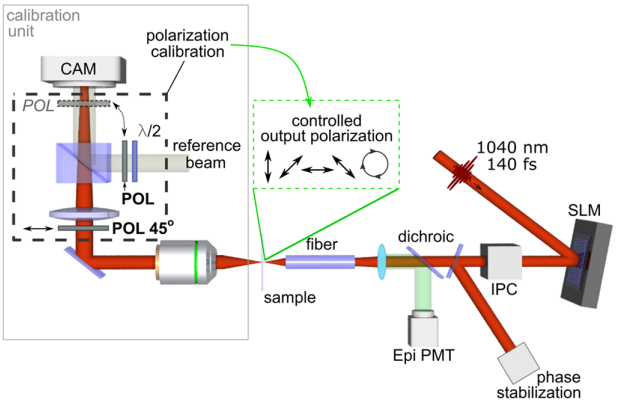

Fig. 1. Experimental setup: λ/2, half wave plate; SLM, spatial light modulator; POL, polarizer (the dashed polarizer is at an alternative position, which gives purer polarization (see main text)); PMT, photomultiplier tube; IPC, input polarization compensation unit. The calibration unit is removed during imaging.

photodiode in conjunction with a polarizer monitored the relative phase between the beams, and any drift was compensated for using the SLM. In contrast to [17], we used a 10 mm achromatic lens, instead of an objective lens, to focus the light on the fiber facet, due to its larger transmission at 1040 nm.

For imaging, light epi-collected through the fiber was reflected off a dichroic mirror (Thorlabs M254C45), filtered using a dichroic mirror (Thorlabs DMLP505), a bandpass filter (Thorlabs FBH520-10) and a shortpass filter (FELH0700) and directed toward a photomultiplier tube (PMT) (Hamamatsu H10723) for detection.

B. Calibration and Output Polarization Control

The characterization of the MMF's light transport is performed by sequentially projecting a set of tightly focused spots onto the core of the proximal fiber facet. For each input point, the speckle pattern at the imaging plane, 15 μm in front of the distal facet of the fiber, was imaged and interfered with the reference beam. The amplitude and phase relative to the reference beam were then retrieved using phase-shifting interferometry. Effectively, each camera pixel represents a location on the imaging plane where a spot can be formed by constructive interference by simultaneously setting the appropriate phase and amplitude for each input point using the SLM.

In order to arbitrarily set the output polarization, two calibrations must be performed, one for each orthogonal output polarization state. For this purpose, a half-wave plate in conjunction with a polarizer is used to change the polarization of the reference beam by 90° between each calibration. Subsequently, the relative phase offset between the output spots can be determined by creating a spot in the same position using both calibrations simultaneously and, utilizing a polarizer between the fiber and the camera set at 45°, making the spots interfere while phase shifting one of them using the SLM to maximize the spot intensity. During imaging, the polarization state of the spot can be set to any linear, circular, or elliptical polarization by setting the relative power and phase of the orthogonally polarized spots. This is done solely by changing the relative amplitude and phase of the two holograms on the SLM. In our setup, a polarization ratio for linearly polarized light of 1:90 was achieved on average (ranging from 1:70 to 1:130). For a circularly polarized spot, the ratio was on average above 0.8:1. It is important to note that in contrast to the relative phase of the *input* polarizations, which needs to be continuously stabilized [17], the relative phase between the spots for the two *output* polarizations only needs to be determined once, during calibration, and it is then stable during the experiment.

The FWHM of the spot at the imaging plane was 1.9 μm, similar to what is expected from the NA of the fiber. The expected resolution for SHG imaging was thus ∼1 μm. The focused spot contained ∼60% of the total laser power at the sample surface, and the rest of the laser power is in a low-intensity speckle pattern across the entire field of view (FOV). This number is often referred to as the power ratio of the spot [33]. In contrast to single-photon imaging, this does not contribute substantially to a background signal because of the quadratic dependence of the SHG signal on the laser power. Because of its low intensity, the speckle pattern likely does not result in additional photobleaching.

C. Technical Limitations of the Scanning Speed

The scan speed of the current implementation of the endoscope is limited by a combination of the signal level and collection efficiency, and the limited update rate of the SLM. A higher NA fiber would increase the generated signal level (at the price of a longer calibration time), and thus would lower the signal collection time. Since the SHG signal is predominantly generated in the forward direction (forward SHG being over 20 times that of backward SHG for tendon and over 425 times for muscle tissue [39]), epi-detection relies on the signal being backscattered from the tissue. The detection of such backscattered light is limited by the size of the detector aperture, which is small for an MMF. Designing the probe to collect light through the cladding or using a somewhat larger diameter probe could increase the detection efficiency. Combining this, submicrosecond per pixel integration times should be feasible. The SLM takes 4–5 ms to form a new hologram and move the beam to the next pixel. During this time no signal is collected. As discussed in [17], potential remedies for that are overdriving the SLM, potentially reaching 1 kHz update rates, and, future developments of faster light modulation devices, e.g., micromirror piston-like microelectromechanical systems (MEMS) systems [40]. Another possible approach to achieving higher scan speeds is to use memory-effect scanning similar to what has been demonstrated for scattering media [28,41–43].

D. Probe Preparation

Nonlinear imaging techniques, such as SHGIM, require short laser pulses to be delivered to the imaging plane. Hence, our MMF endoscope is based on GRIN MMFs, since they have a larger bandwidth (and lower modal dispersion) when compared to their step index counterparts [33]. This minimizes the pulse length (the pulse length at the sample plane is <400 fs) and maximizes the power in the spot. Moreover, GRIN MMFs have been shown to preserve to a high degree their light transport characteristics when bent [44]. The GRIN MMF is a custom-drawn fiber with an NA of 0.3 (drawn at CREOL, UCF), a cladding diameter of 125 μm and a core diameter of 62.5 μm. The fiber is stripped, cleaved, and cut to flat faceted 3 cm pieces. The distal end, i.e., the end going into samples, can be polished into a 45° cone tip for ease of insertion. The angled tip also helps keep tissue residue from sticking onto the facet. The quality of the spot and FOV are not appreciably affected by the polishing. Each probe is glued into a ferrule.

E. Sample Preparation

The mouse tail and heart used for the imaging experiments were harvested from paraformaldehyde (PFA) perfusion-fixed adult mice (wild type and STOCK Tg(Thy1-EGFP)MJrs/J, neither of which are expected to have defects in the collagen structure). The sample acquisition procedures followed the Czech guidelines for animal experimentation and was approved by the Branch Commission for Animal Welfare of the Ministry of Agriculture of the Czech Republic (permission No 47/2020). The samples were further postfixed in 4% PFA in phosphate-buffered saline (PBS) for 24–48 h and then stored in PBS until imaging. Tail sections were skinned and glued to a Petri dish prior to imaging. The heart was halved along the sagittal plane and held in place using a base of 1.5% agarose in PBS. The samples were kept submerged in PBS for imaging.

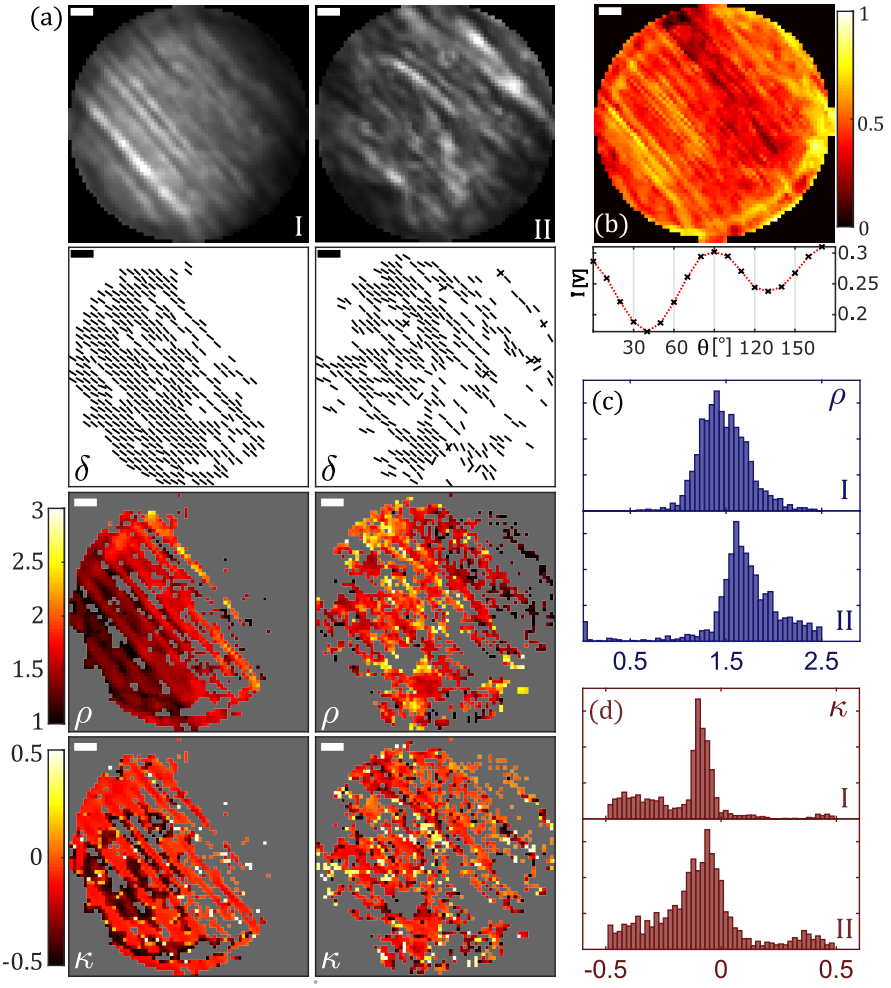

Fig. 2. Results from linear polarization SHGIM on mouse tail tendon for two imaging areas (I and II). (a) From top to bottom, sum of the intensity for all polarization angles, quiver plot of fibril in-plane orientation δ, and parameter maps for ρ and κ from imaging areas I (left) and II (right); (b) modulation depth for area I and mean signal intensity for the entire FOV; (c) and (d) histograms for ρ and κ, respectively, in imaging areas I and II. Quiver plots were binned (2:1) for improved visualization of the fibril orientation. All scale bars are 5 μm.

F. Imaging

The power in the focused spot ranged from 50 to 300 mW, depending on signal strength. The spot was raster-scanned across the sample with a pixel integration time in the span of 2 to 12 ms. The PMT signal was collected using a National Instruments (NI) data aquisition (DAQ) card and averaged over this time. The images of the tail were taken at the tissue surface. Since the probe did not pierce the tissue, a probe with a flat facet was used. The heart was pierced with the fiber itself (polished into a cone tip), and imaging was done within the myocardium. The pericardium was imaged before piercing the tissue. With a 2 ms integration time, we achieved a scanning speed of about 150 pixels per second, each image taking between 30 and 80 s depending on the pixel step. Power fluctuations resulting from changing the polarization in the spot were found to be ∼4% and were compensated for prior to performing the data analysis. Also, placing the polarizer in front of the camera, in the beam path common to the signal and reference, instead of in the reference path (see Fig. 1) during the calibration procedure improves circular polarization purity and uniformity across the FOV, making this the preferred configuration for SHG CD imaging, which is sensitive to small deviations from circular polarization.

The imaging parameters for the data presented in Figs. 2–6 were as follows: For the mouse tail tendon, the number of polarization values used per area ranged from 12 to 18, and the pixel integration time was 2 ms. The pixel step was 0.53 μm for areas III and IV and 0.79 μm for the rest. For muscle tissue adjacent to the tendon, the pixel step was 0.79 μm. The laser power in the focused spot was ∼60 mW.

For the heart, 12 images with different polarization directions were taken in each area. Since the signal from the myocardium was substantially weaker than the signal from collagen, longer pixel integration times were used. Pixel dwell times were 2, 8, and 12 ms, and pixel step sizes were 0.79, 0.53, and 1.05 μm for areas I, II, and III, respectively. The laser power in the focused spot was ∼120 mW.

G. Linear Polarization SHGIM

This technique consists in the acquisition of a series of consecutive images, each at a different linear polarization angle. The modulation of the excitation polarization angle results in an amplitude modulation of the SHG signal, I_{SHG}, which will be governed by the effective second-order nonlinear susceptibility tensor, $\chi^{(2)}$, of the sample. By fitting a mathematical model to the data, $\chi^{(2)}$

and the orientation of the fibril can be probed. For this work, we utilized the C_6 symmetry model proposed by Golaraei *et al.* [45] that describes the dependence of I_{SHG} on the effective $\chi^{(2)}$; in-plane fibril orientation, δ; out-of-plane fibril orientation, α; linear polarization angle of the exciting illumination, θ; and the detected light polarization angle, ϕ:

$$I_{SHG} \propto \left|\rho \sin(\phi-\delta)\sin 2(\theta-\delta) + \cos(\phi-\delta)\sin^2(\theta-\delta) + \nu\cos(\phi-\delta)\cos^2(\theta-\delta) + 2\kappa\cos(\theta-\delta)\sin(\theta-\phi)\right|^2,$$

$$\rho = \frac{\chi^{(2)}_{zzz}}{\chi^{(2)}_{zxx}}\cos^2(\alpha) + 3\sin^2(\alpha),\ \kappa = \frac{\chi^{(2)}_{xyz}}{\chi^{(2)}_{zxx}}\sin(\alpha),\ \nu = \frac{\chi^{(2)}_{xxz}}{\chi^{(2)}_{zxx}} \approx 1. \quad (1)$$

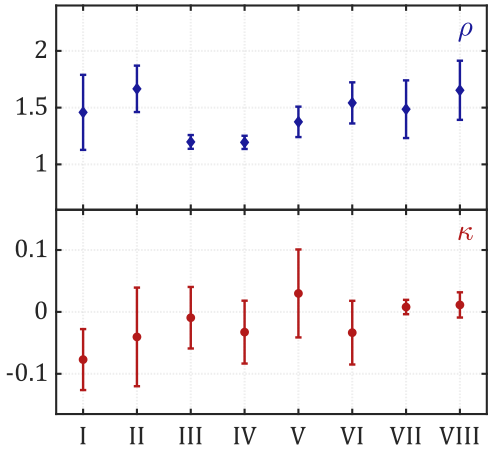

Fig. 3. Peak locations for ρ and κ for linear polarization SHGIM performed on eight different imaging areas on tendon from a mouse tail. Error bars denote the standard deviation.

For this work, we have assumed $\nu = 1$, a valid approximation when the second-harmonic emitter is rod-like [46], as for a fibril segment. Since GRIN fibers do not completely preserve the polarization of the transmitted light, we detect and model the total intensity given by

$$I_{Total} \propto I_{\phi=0} + I_{\phi=\pi/2}. \quad (2)$$

This results in the loss of a known dimension in the search space and can be unfavorable for any fitting attempts; however, as long as the quadrant of the in-plane fibril orientation is known, δ, κ, and ρ can still be determined.

The parameter κ depends on the chirality of the sample and the out-of-plane tilt [45]. For an in-plane fibril, $\kappa = 0$, resulting in a model equivalent to the C_{6v} symmetry model, employed in several previous works [34,47], and in this case, $\rho = \chi^{(2)}_{zzz}/\chi^{(2)}_{zxx}$, reflecting only the material proprerties. The C_6 symmetry model is better suited for endoscopic imaging where the orientation of the fibrils cannot be assumed to be parallel to the imaging plane. Although birefringence is neglected in this model, imaging near the fiber facet helps mitigate, although not nullify, its effects [48].

3. RESULTS

We performed polarization-resolved SHGIM on mouse tail tendon and muscle to validate the ability to differentiate collagen and myosin and imaged the myocardium of fixed heart tissue, inserting the endoscope to a depth >1 mm to demonstrate the capability for imaging at depth.

A. Mouse Tail

Linear polarization SHGIM was first tested on muscle and tendon using the exposed tissue of a skinned mouse tail. Tendon is a common test target for SHGIM because of its well-ordered and easily identifiable collagen structure, making it a good sample for

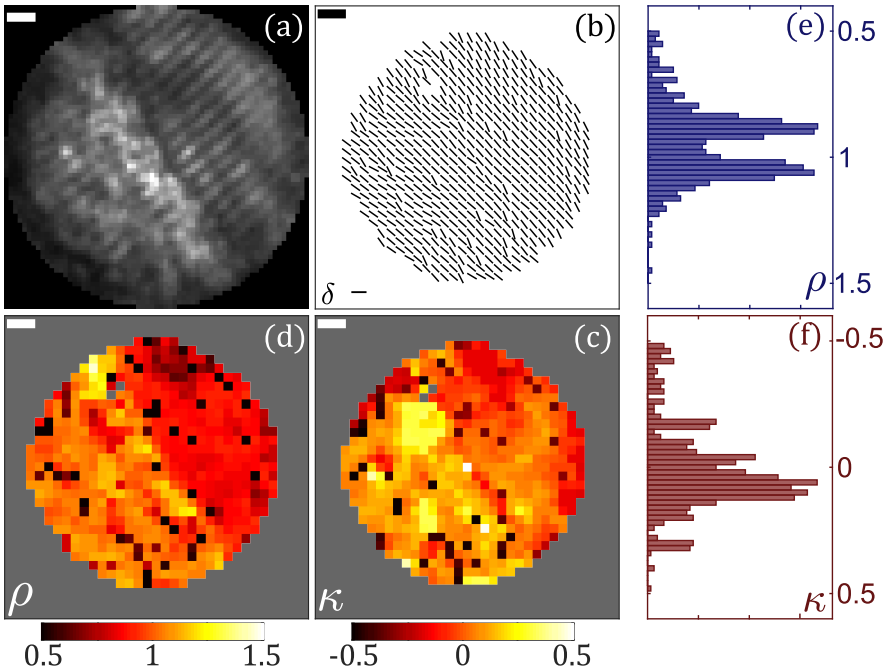

Fig. 4. Results from linear polarization SHGIM on muscle tissue. (a) Sum of intensities for all polarization angles; (b) quiver plot of fibril in-plane orientation δ; (c) and (d) parameter maps for κ and ρ; (e) and (f) histograms for ρ and κ. All scale bars are 5 μm.

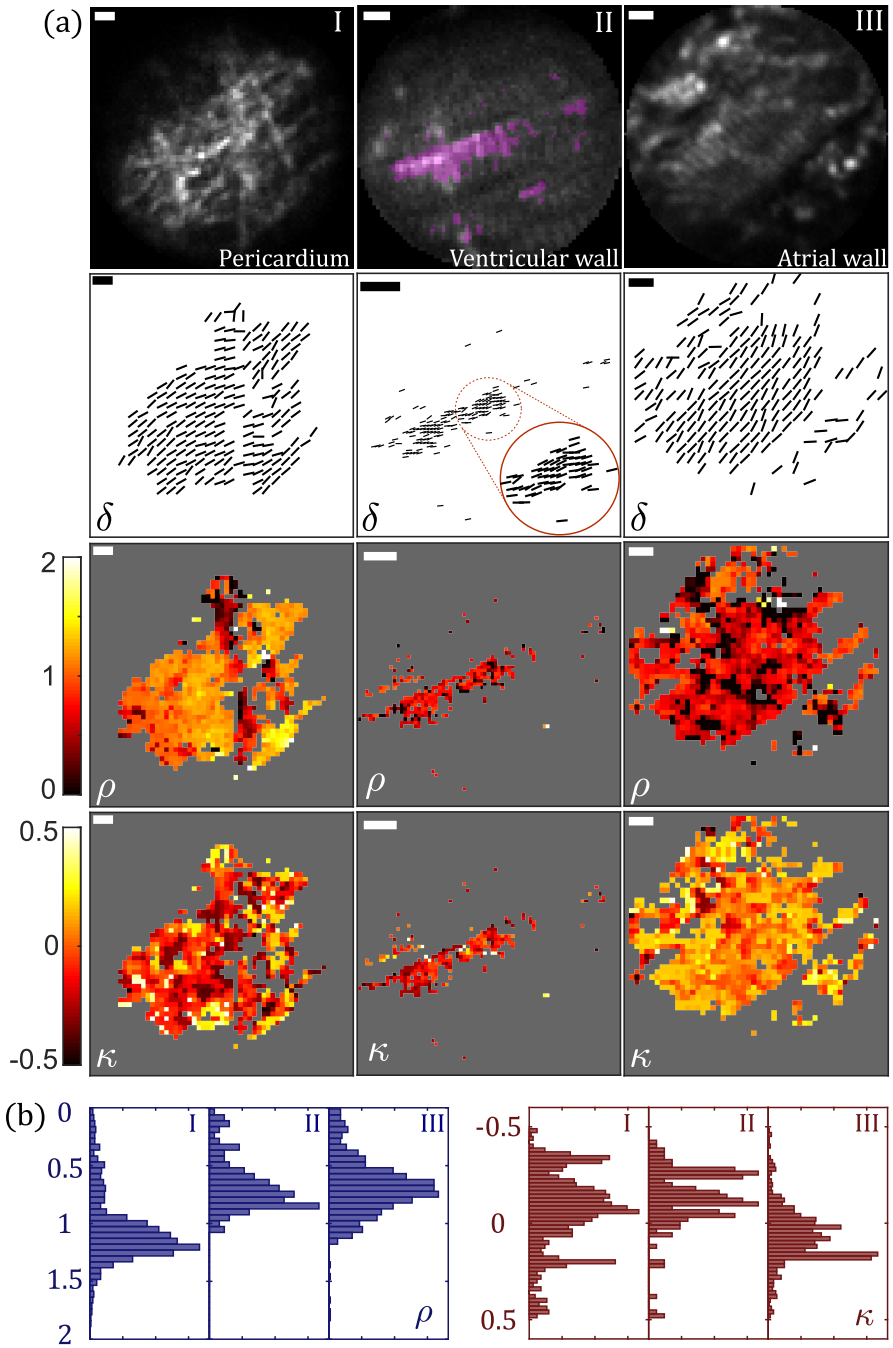

Fig. 5. Results from linear polarization SHGIM of a mouse heart for three different positions (I, pericardium; II, ventricular wall; and III, atrial wall). (a) From top to bottom, sum of the SHG intensity for left- and right-handed circularly polarized excitation, in-plane orientation δ, ρ and κ parameter maps; (b) ρ and κ histograms. All scale bars are 5 μm.

the validation of the MMF endoscope. The MMF was placed at the calibrated working distance (∼15 μm) above a section of the tail, which was laid horizontally on the sample holder. Measurements were taken at eight different areas on exposed tendon from three sections from two different tails.

The images were analyzed as follows: Since excessive noise in the signal can lead to local minima in the fit becoming problematic, prior to fitting, each image is denoised using a 2 × 2 median filter. Images from some areas (detailed below) were additionally downsampled using bicubic interpolation in a ratio 3:2 to obtain a cleaner signal. Then, the subset of pixels where the modulation depth of the signal was >30% were selected [see Fig. 2(b)]. Equation (2) was then fitted to the data using a multiple start point trust-region algorithm using the optimization toolbox version 8.2 in MATLAB 2018b. The plot in Fig. 2(b) shows the normalized intensity and the fit for the pixel marked with an "×". The fit bounds were $-0.5 \le \kappa \le 0.5$ and $0 \le \rho \le 3$. Pixels resulting in a fit to one or more of the bound values were discarded, as were those with a coefficient of determination, R^2, of less than 0.8. The results from the fits were then used to create parameter maps for δ, ρ, and κ. The characteristic values for ρ and κ for the sample were

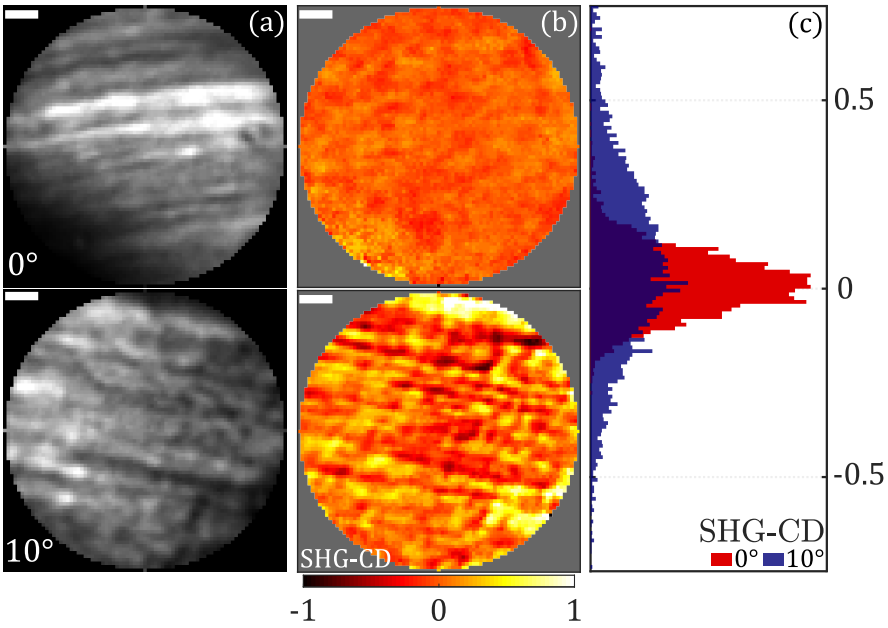

Fig. 6. Results from SHG CD imaging of a tilted and in-plane sample of mouse tail tendon. (a) Sum of the SHG intensity from left- and right-handed circularly polarized excitation; (b) SHG CD maps; (c) SHG CD histogram. The tilted and in-plane images were taken from two different areas within the same tail section. All scale bars are 5 μm.

determined by plotting a histogram of the parameter and fitting a normal distribution to five bins on each side of the maximal value.

In Figs. 2(a), 2(c), and 2(d), we see the results from the analysis performed for two different imaging areas (I and II) on the tendon. Figure 2(a) shows, from top to bottom, the sum of the image intensities for all polarization angles, a quiver plot for the in-plane orientation of the fibrils, δ, and the ρ and κ parameter maps, indicating the tissue composition and out-of-plane tilt of the fibrils, respectively. The strong alignment of the collagen in tendon can be clearly seen from the quiver plot of δ. The upper right-hand corner of the sample is out of focus because the sample is a thick tissue slice, which is not flat, and the endoscope is placed above the tissue slice. Figures 2(c) and 2(d), respectively, show the histograms for ρ and κ. For area I, $\rho = 1.46 \pm 0.33$ and for area II, $\rho = 1.68 \pm 0.22$, consistent with reports for collagen [49–51]. The histogram for parameter κ peaked at -0.08 ± 0.05 in area I and -0.06 ± 0.11 in area II, consistent with fibrils exhibiting modest tilts. The analysis results from all eight imaged areas are summarized in Fig. 3. For areas III, IV, and V, bicubic interpolation was used prior to fitting. The characteristic values for κ were all consistent with horizontally oriented samples exhibiting modest tilts of the fibrils. Therefore, $\rho \approx \chi^{(2)}_{zzz}/\chi^{(2)}_{zxx}$ and indeed, ρ coincides with reports for $\chi^{(2)}_{zzz}/\chi^{(2)}_{zxx}$ values for collagen Type I [49–51], the main constituent of tendons.

Additionally, a measurement was taken on muscle tissue adjacent to the tendon. The muscle was identifiable due to its characteristic striation. The SHG signal from this area was an order of magnitude lower than the signal from collagen, and to compensate for the noisier signal the images were downsampled using bicubic interpolation prior to fitting. The results are shown in Fig. 4. The alignment of the myofibrils is reflected in the δ plot [Fig. 4(b)]. In the ρ map in Fig. 4(d), we can observe two distinct regions, which can also be seen as two distinct peaks in the histogram for ρ. The peak value for κ at 0.08 ± 0.11 suggests a modest tilt of the myofibrils, and thus ρ should be comparable to $\chi^{(2)}_{zzz}/\chi^{(2)}_{zxx}$ and thus reflect only the sample composition. Indeed, the first ρ peak at 0.89 ± 0.06 is in the range of literature reports for myosin [52], the protein responsible for SHG in muscle. The second peak at 1.06 ± 0.07 likely indicates the inclusion of collagen in the tissue [52]. If a mix of muscle and collagen are responsible for the SHG signal in a given pixel, ρ would result in an intermediate value from the superimposed signals.

B. Mouse Heart

Next, we performed linear polarization SHGIM on a mouse heart to validate the MMF endoscope in tissue-imaging capabilities. Here, we first acquired images using circular polarization to produce SHG in the fibrils, regardless of the orientation, and locate an imaging target. Once an area of interest was located, we proceeded to acquire linear polarization SHGIM images by varying the polarization angle and analyzed the data as for the mouse tail sample.

Figure 5 shows results obtained for three different imaging areas (I, II, and III) in the mouse heart. Since the scanning method is SLM-based, we can access the pixels in any order desired, and it is straightforward to choose a region of interest (ROI) of an arbitrary shape as shown in area II [Fig. 5(a)]. The scanned area is highlighted in magenta and represents the pixels whose intensity exceeded 25% of the maximum intensity from the initial scan using circular polarization. This allows us to study finer details in an ROI while keeping the scan time reasonable.

Figure 5(b) shows the histograms for ρ and κ, respectively. Unlike in the tail tendon sample, the fibrils in the heart cannot be expected to be in-plane, which is reflected by $\kappa \neq 0$, which means that $\rho > \chi^{(2)}_{zzz}/\chi^{(2)}_{zxx}$, that is, the value of ρ is not solely dependent on the material and structure of the fibril, but also its out-of-plane orientation. Imaging area I was located at the heart's surface. The outer layer of the heart, the pericardium, consists of a collagenous structure, and the location of the ρ peak, 1.18 ± 0.19, is within

the range of values reported for collagen in the literature [51]. Imaging area II was inside the right ventricular wall, while area III was within the right atrial wall at a depth between 800 and 1000 μm. In the histograms for ρ, peaks are seen at 0.79 ± 0.19 for the ventricular wall and at 0.74 ± 0.23 for the atrial wall, still within range of the literature values for $\chi^{(2)}_{zzz}/\chi^{(2)}_{zxx}$ for myosin [26,47]. As expected, we observed local alignment of the in-plane orientation of the fibrils, δ, but less long-range order than seen in the tail tendon sample.

C. SHG CD

Our method is not limited to linear polarization, but any in-plane polarization state can be created. This allows measurements of the SHG CD, a quantity, like κ, tied to the chirality of the sample and sensitive to the out-of-plane tilt [34]. Normalized SHG CD is defined as $2(I_{\mathrm{RHCP}} - I_{\mathrm{LHCP}})/(I_{\mathrm{RHCP}} + I_{\mathrm{LHCP}})$ [53].

We demonstrated SHG CD imaging on a section of the mouse tail, which was initially lying flat on the sample holder. The probe was placed above the exposed tendon, and two images were acquired, using LHC and RHC polarization excitation. Then, the sample was tilted by an angle, α, of approximately 10°, resulting in the tendons being tilted 10° out of the imaging plane, and another set of images was taken. During the tilting, the sample was moved so the images are not of the same area, but lie within the same general section. SHG CD was then calculated for each area.

Results are shown in Fig. 6. Clearly, the 10° tilt resulted in an increase in the SHG CD contrast when compared with the in-plane sample. This can also be seen in the histogram in Fig. 6(c), where the SHG CD signal distributions had a standard deviation of 0.11 for the in-plane sample and 0.33 for the tilted sample. In general, a nonzero SHG CD magnitude is indicative of an out-of-plane tilt in samples where the chiral component $\chi^{(2)} \neq 0$. The sign of the SHG CD depends on the sign and magnitudes of the chiral terms of $\chi^{(2)}$ but also on the sign of the tilt angle α. A change in only the sign of the contrast may be understood as flipping the fibril by $\alpha = 180°$ [34,54], although the interpretation must be made with caution [55].

4. DISCUSSION

As the excitation is at 1040 nm (which is a useful wavelength for SHG because of the availability of powerful lasers), the detected signal is at 520 nm, which is in the green wavelength range. In this wavelength range, biological samples often exhibit strong autofluorescence. This is, however, not a large problem for polarization-resolved SHGIM, since the autofluorescence signal is not modulated with the polarization, although care must be taken to properly characterize the polarization of the output spot, as optics such as dichroic mirrors, which have a polarization-dependent reflectivity might otherwise introduce an artificial polarization dependence of the signal [56]. In this paper, we have chosen not to analyze the pixels that had a low modulation depth, indicative of a significant autofluorescence background. Although a strong fluorescence signal results in excess noise in the modulated SHG signal, making fitting and detailed analysis difficult, it still clear what fraction of the signal is SHG, and it removes the risk of mislabeling autofluorescent structures as collage, myosin, etc.

The excitation powers used here were comparable to those for SHG imaging in lens-based endoscopes. The total integration time for all polarization directions was 5-10 times longer, as expected from the low NA (0.3) of the MMF and small collection aperture. As discussed in the Materials and Methods section, we expect to be able to partly remedy this with a higher NA fiber and a slightly larger diameter probe.

As we see in the measurements on the tail muscle, the method reveals when there is a mixture of materials in the sample [57]. This would allow an indication of the collagen content in the tissue, even if we here do not image in enough detail to resolve, for instance, thin collagen strands found in healthy heart tissue [19]. Furthermore, the method actually has the potential of distinguishing collagen I and collagen II [58] and selectively images fibrillar collagen, since nonfibrillar collagen (e.g., Type IV) does not generate SHG. Additionally, dynamic processes in the muscle tissue could potentially be studied, since the ρ parameter is sensitive to the conformation of the myosin molecule and thus the physiological state of muscle tissue [8].

The parameters ρ and κ cannot be completely decoupled in this implementation of the method, unless the chirality has been measured separately. In some instances, this could confuse a mixed material with a fibril tilted out-of-plane. Nevertheless, it is clear from the nonzero value for κ that the fibril is tilted, although the exact angle cannot be quantified. For images where even a small subset of pixels shows $\kappa \approx 0$, the subset can be selected and used to estimate $\chi^{(2)}_{zzz}/\chi^{(2)}_{zxx}$. These pixels could alternatively be selected from an SHG CD image of the same sample area. Furthermore, for many clinical applications, a scoring system is used, where the range of values or combinations of multiple values (e.g., fluorescence intensity and SHG parameters) relative to a healthy specimen indicate whether the tissue is diseased or not. For these applications, the coupling of ρ and κ is likely less important.

As mentioned above, our method allows scanning in an arbitrary pixel order. In addition to allowing selection of arbitrarily shaped and disjoint ROIs, it is easy to swap the scan order, to use all the polarization values for a single pixel before moving onto the next. This could improve SHG CD imaging, which is prone to drift-related artifacts [53]. We would get the correct CD value in each pixel, even if the sample drifts. SHG CD has shown potential relevance for the study of pathologies such as pulmonary fibrosis [35] and ovarian cancer [36]. Since it only requires two images to be acquired, it is faster, and a more robust implementation might make it more attractive for diagnostic purposes.

SHGIM can be used as a part of nonlinear multimodal imaging through an MMF, together with CARS [17] and two-photon fluorescence [18]. The setup is completely compatible with such multimodal imaging. As we discuss in [17,33], wavelength tuning within a small range around the calibration wavelength can be accommodated using a dispersive prism in front of the fiber, and for well-separated excitation wavelengths, e.g., for fluorescence and SHG, an MMF calibration step can be done for each wavelength. If improvements in the scan speed (see Section 2.D) are implemented, this could be an avenue towards *in situ* tumor diagnosis, e.g., differentiating gliomas from healthy brain tissue [5,59], where a minimally invasive endoscope would be an asset.

5. CONCLUSION

In conclusion, we have shown that it is possible to perform SHG microscopy in a minimally invasive fashion through an MMF endoscope. Moreover, we can fully control the in-plane polarization state of the scanning focus at the fiber output, and we use this to implement linearly polarized SHGIM and SHG CD imaging.

By imaging fixed mouse tail tendon and muscle as well as heart tissue, we verify that we, through the polarization modulation, achieve contrast between the structural proteins myosin and collagen at a single-pixel level. Furthermore, we can detect the local orientation of the collagen fibrils. We demonstrate that the imaging can be performed at a depth of 1 mm into the heart tissue since the endoscope can be inserted to any depth well beyond light penetration depth in the tissue. We believe that this work is a step toward a device capable of performing label-free diagnostics of tumors and fibrotic diseases *in situ* and at depths not accessible *in vivo* with currently available microscopy techniques.

Funding. European Regional Development Fund (CZ.02.1.01/0.0/0.0/15_003/0000476, CZ.1.05/2.1.00/01.0017); Ministerstvo Školství, Mládeže a Tělovýchovy (LO1212); European Research Council (724530); Akademie Věd České Republiky (RVO:68081731); National Science Foundation (ECCS-1711230).

Acknowledgment. Petr Jákl and Martin Šiler are acknowledged for the development of the camera toolbox and CUDA library for hologram generation, respectively.

Disclosures. The authors declare no conflicts of interest.

Data Availability. Data underlying the results presented in this paper are available in Ref. [60].

REFERENCES

1. T. D. Wang and J. Van Dam, "Optical biopsy: a new frontier in endoscopic detection and diagnosis," Clin. Gastroenterol. Hepatol. **2**, 744–753 (2004).
2. T. W. Bocklitz, F. S. Salah, N. Vogler, S. Heuke, O. Chernavskaia, C. Schmidt, M. J. Waldner, F. R. Greten, R. Bräuer, and M. Schmitt, "Pseudo-HE images derived from CARS/TPEF/SHG multimodal imaging in combination with Raman-spectroscopy as a pathological screening tool," BMC Cancer **16**, 1–11 (2016).
3. T. Hollon and D. A. Orringer, "Label-free brain tumor imaging using Raman-based methods," J. Neuro-Oncol. **151**, 393–402 (2021).
4. K. He, L. Zhao, Y. Chen, X. Huang, Y. Ding, H. Hua, L. Liu, X. Wang, M. Wang, and Y. Zhang, "Label-free multiphoton microscopic imaging as a novel real-time approach for discriminating colorectal lesions: a preliminary study," J. Gastroenterol. Hepatol. **34**, 2144–2151 (2019).
5. N. Fang, Z. Wu, X. Wang, N. Cao, Y. Lin, L. Li, Y. Chen, S. Cai, H. Tu, and D. Kang, "Rapid, label-free detection of intracranial germinoma using multiphoton microscopy," Neurophotonics **6**, 035014 (2019).
6. P. J. Campagnola and C. Y. Dong, "Second harmonic generation microscopy: principles and applications to disease diagnosis," Laser Photon. Rev. **5**, 13–26 (2011).
7. L. Gailhouste, Y. Le Grand, C. Odin, D. Guyader, B. Turlin, F. Ezan, Y. Désille, T. Guilbert, A. Bessard, and C. Frémin, "Fibrillar collagen scoring by second harmonic microscopy: a new tool in the assessment of liver fibrosis," J. Hepatol. **52**, 398–406 (2010).
8. V. Nucciotti, C. Stringari, L. Sacconi, F. Vanzi, L. Fusi, M. Linari, G. Piazzesi, V. Lombardi, and F. Pavone, "Probing myosin structural conformation in vivo by second-harmonic generation microscopy," Proc. Natl. Acad. Sci. USA **107**, 7763–7768 (2010).
9. A. Lombardini, V. Mytskaniuk, S. Sivankutty, E. R. Andresen, X. Chen, J. Wenger, M. Fabert, N. Joly, F. Louradour, and A. Kudlinski, "High-resolution multimodal flexible coherent Raman endoscope," Light Sci. Appl. **7**, 10 (2018).
10. A. Lukic, S. Dochow, H. Bae, G. Matz, I. Latka, B. Messerschmidt, M. Schmitt, and J. Popp, "Endoscopic fiber probe for nonlinear spectroscopic imaging," Optica **4**, 496–501 (2017).
11. I. M. Vellekoop and A. Mosk, "Focusing coherent light through opaque strongly scattering media," Opt. Lett. **32**, 2309–2311 (2007).
12. S. M. Popoff, G. Lerosey, R. Carminati, M. Fink, A. C. Boccara, and S. Gigan, "Measuring the transmission matrix in optics: an approach to the study and control of light propagation in disordered media," Phys. Rev. Lett. **104**, 100601 (2010).
13. S. Sivankutty, E. R. Andresen, R. Cossart, G. Bouwmans, S. Monneret, and H. Rigneault, "Ultra-thin rigid endoscope: two-photon imaging through a graded-index multi-mode fiber," Opt. Express **24**, 825–841 (2016).
14. S. Ohayon, A. Caravaca-Aguirre, R. Piestun, and J. J. DiCarlo, "Minimally invasive multimode optical fiber microendoscope for deep brain fluorescence imaging," Biomed. Opt. Express **9**, 1492–1509 (2018).
15. S. Turtaev, I. T. Leite, T. Altwegg-Boussac, J. M. Pakan, N. L. Rochefort, and T. Čižmár, "High-fidelity multimode fibre-based endoscopy for deep brain in vivo imaging," Light Sci. Appl. **7**, 92 (2018).
16. S. A. Vasquez-Lopez, R. Turcotte, V. Koren, M. Plöschner, Z. Padamsey, M. J. Booth, T. Čižmár, and N. J. Emptage, "Subcellular spatial resolution achieved for deep-brain imaging in vivo using a minimally invasive multimode fiber," Light Sci. Appl. **7**, 110 (2018).
17. J. Trägårdh, T. Pikálek, M. Šerý, T. Meyer, J. Popp, and T. Čižmár, "Label-free CARS microscopy through a multimode fiber endoscope," Opt. Express **27**, 30055–30066 (2019).
18. E. Kakkava, M. Romito, D. B. Conkey, D. Loterie, K. M. Stankovic, C. Moser, and D. Psaltis, "Selective femtosecond laser ablation via two-photon fluorescence imaging through a multimode fiber," Biomed. Opt. Express **10**, 423–433 (2019).
19. T. P. Martin, G. Norris, G. McConnell, and S. Currie, "A novel approach for assessing cardiac fibrosis using label-free second harmonic generation," Int. J. Cardiovasc. Imaging **29**, 1733–1740 (2013).
20. F. J. Ávila, O. Del Barco, and J. M. Bueno, "Quantifying external and internal collagen organization from Stokes-vector-based second harmonic generation imaging polarimetry," J. Opt. **19**, 105301 (2017).
21. G. Recher, D. Rouede, P. Richard, A. Simon, J.-J. Bellanger, and F. Tiaho, "Three distinct sarcomeric patterns of skeletal muscle revealed by SHG and TPEF microscopy," Opt. Express **17**, 19763–19777 (2009).
22. D. A. Dombeck, K. A. Kasischke, H. D. Vishwasrao, M. Ingelsson, B. T. Hyman, and W. W. Webb, "Uniform polarity microtubule assemblies imaged in native brain tissue by second-harmonic generation microscopy," Proc. Natl. Acad. Sci. USA **100**, 7081–7086 (2003).
23. R. Cicchi, N. Vogler, D. Kapsokalyvas, B. Dietzek, J. Popp, and F. S. Pavone, "From molecular structure to tissue architecture: collagen organization probed by SHG microscopy," J. Biophoton. **6**, 129–142 (2013).
24. D. Tokarz, R. Cisek, A. Joseph, S. L. Asa, B. C. Wilson, and V. Barzda, "Characterization of pathological thyroid tissue using polarization-sensitive second harmonic generation microscopy," Lab. Investig. **100**, 1280–1287 (2020).
25. A. Golaraei, L. B. Mostaço-Guidolin, V. Raja, R. Navab, T. Wang, S. Sakashita, K. Yasufuku, M.-S. Tsao, B. C. Wilson, and V. Barzda, "Polarimetric second-harmonic generation microscopy of the hierarchical structure of collagen in stage I-III non-small cell lung carcinoma," Biomed. Opt. Express **11**, 1851–1863 (2020).
26. C. Odin, T. Guilbert, A. Alkilani, O. P. Boryskina, V. Fleury, and Y. Le Grand, "Collagen and myosin characterization by orientation field second harmonic microscopy," Opt. Express **16**, 16151–16165 (2008).
27. D. Rouède, E. Schaub, J.-J. Bellanger, F. Ezan, J.-C. Scimeca, G. Baffet, and F. Tiaho, "Determination of extracellular matrix collagen fibril architectures and pathological remodeling by polarization dependent second harmonic microscopy," Sci. Rep. **7**, 12197 (2017).
28. H. B. de Aguiar, S. Gigan, and S. Brasselet, "Polarization recovery through scattering media," Sci. Adv. **3**, e1600743 (2017).
29. Y. Guan, O. Katz, E. Small, J. Zhou, and Y. Silberberg, "Polarization control of multiply scattered light through random media by wavefront shaping," Opt. Lett. **37**, 4663–4665 (2012).
30. S. Tripathi, R. Paxman, T. Bifano, and K. C. Toussaint, "Vector transmission matrix for the polarization behavior of light propagation in highly scattering media," Opt. Express **20**, 16067–16076 (2012).
31. W. Xiong, C. W. Hsu, Y. Bromberg, J. E. Antonio-Lopez, R. A. Correa, and H. Cao, "Complete polarization control in multimode fibers with polarization and mode coupling," Light Sci. Appl. **7**, 54 (2018).
32. T. Čižmár and K. Dholakia, "Shaping the light transmission through a multimode optical fibre: complex transformation analysis and applications in biophotonics," Opt. Express **19**, 18871–18884 (2011).
33. T. Pikálek, J. Trägårdh, S. Simpson, and T. Čižmár, "Wavelength dependent characterization of a multimode fibre endoscope," Opt. Express **27**, 28239–28253 (2019).

34. H. Lee, M. J. Huttunen, K.-J. Hsu, M. Partanen, G.-Y. Zhuo, M. Kauranen, and S.-W. Chu, "Chiral imaging of collagen by second-harmonic generation circular dichroism," Biomed. Opt. Express **4**, 909–916 (2013).
35. D. S. James, A. N. Jambor, H.-Y. Chang, Z. Alden, K. B. Tilbury, N. K. Sandbo, and P. J. Campagnola, "Probing ECM remodeling in idiopathic pulmonary fibrosis via second harmonic generation microscopy analysis of macro/supramolecular collagen structure," J. Biomed. Opt. **25**, 014505 (2019).
36. K. R. Campbell, R. Chaudhary, J. M. Handel, M. S. Patankar, and P. J. Campagnola, "Polarization-resolved second harmonic generation imaging of human ovarian cancer," J. Biomed. Opt. **23**, 066501 (2018).
37. S. J. Baskey, M. Andreana, E. Lanteigne, A. Ridsdale, A. Stolow, and M. E. Schweitzer, "Pre-clinical translation of second harmonic microscopy of meniscal and articular cartilage using a prototype nonlinear microendoscope," IEEE J. Transl. Eng. Health Med. **7**, 1–11 (2018).
38. M. E. Llewellyn, R. P. Barretto, S. L. Delp, and M. J. Schnitzer, "Minimally invasive high-speed imaging of sarcomere contractile dynamics in mice and humans," Nature **454**, 784–788 (2008).
39. F. Légaré, C. Pfeffer, and B. R. Olsen, "The role of backscattering in SHG tissue imaging," Biophys. J. **93**, 1312–1320 (2007).
40. V. Shrauger and C. Warde, "Development of a high-speed high-fill-factor phase-only spatial light modulator," Proc. SPIE **4291**, 101–108 (2001).
41. L. V. Amitonova, A. P. Mosk, and P. W. Pinkse, "Rotational memory effect of a multimode fiber," Opt. Express **23**, 20569–20575 (2015).
42. S. Li, S. A. Horsley, T. Tyc, T. Čižmár, and D. B. Phillips, "Memory effect assisted imaging through multimode optical fibres," Nat. Commun. **12**, 3751 (2021).
43. N. Stasio, D. B. Conkey, C. Moser, and D. Psaltis, "Light control in a multicore fiber using the memory effect," Opt. Express **23**, 30532–30544 (2015).
44. D. E. B. Flaes, J. Stopka, S. Turtaev, J. F. De Boer, T. Tyc, and T. Čižmár, "Robustness of light-transport processes to bending deformations in graded-index multimode waveguides," Phys. Rev. Lett. **120**, 233901 (2018).
45. A. Golaraei, K. Mirsanaye, Y. Ro, S. Krouglov, M. K. Akens, B. C. Wilson, and V. Barzda, "Collagen chirality and three-dimensional orientation studied with polarimetric second-harmonic generation microscopy," J. Biophoton. **12**, e201800241 (2019).
46. C. A. Dailey, B. J. Burke, and G. J. Simpson, "The general failure of Kleinman symmetry in practical nonlinear optical applications," Chem. Phys. Lett. **390**, 8–13 (2004).
47. F. Tiaho, G. Recher, and D. Rouède, "Estimation of helical angles of myosin and collagen by second harmonic generation imaging microscopy," Opt. Express **15**, 12286–12295 (2007).
48. D. Aït-Belkacem, A. Gasecka, F. Munhoz, S. Brustlein, and S. Brasselet, "Influence of birefringence on polarization resolved nonlinear microscopy and collagen SHG structural imaging," Opt. Express **18**, 14859–14870 (2010).
49. P.-J. Su, W.-L. Chen, Y.-F. Chen, and C.-Y. Dong, "Determination of collagen nanostructure from second-order susceptibility tensor analysis," Biophys. J. **100**, 2053–2062 (2011).
50. A. E. Tuer, M. K. Akens, S. Krouglov, D. Sandkuijl, B. C. Wilson, C. M. Whyne, and V. Barzda, "Hierarchical model of fibrillar collagen organization for interpreting the second-order susceptibility tensors in biological tissue," Biophys. J. **103**, 2093–2105 (2012).
51. E. I. Romijn, A. Finnøy, and M. B. Lilledahl, "Analyzing the feasibility of discriminating between collagen types I and II using polarization-resolved second harmonic generation," J. Biophoton. **12**, e201800090 (2019).
52. W.-L. Chen, T.-H. Li, P.-J. Su, C.-K. Chou, P. T. Fwu, S.-J. Lin, D. Kim, P. T. So, and C.-Y. Dong, "Second harmonic generation χ tensor microscopy for tissue imaging," Appl. Phys. Lett. **94**, 183902 (2009).
53. M. Schmeltz, C. Teulon, G. Latour, D. Ghoubay, V. Borderie, C. Aimé, and M.-C. Schanne-Klein, "Implementation of artifact-free circular dichroism SHG imaging of collagen," Opt. Express **27**, 22685–22699 (2019).
54. A. Golaraei, L. Kontenis, K. Mirsanaye, S. Krouglov, M. K. Akens, B. C. Wilson, and V. Barzda, "Complex susceptibilities and chiroptical effects of collagen measured with polarimetric second-harmonic generation microscopy," Sci. Rep. **9**, 12488 (2019).
55. M. Schmeltz, C. Teulon, M. Pinsard, U. Hansen, M. Alnawaiseh, D. Ghoubay, V. Borderie, G. Mosser, C. Aimé, and F. Légaré, "Circular dichroism second-harmonic generation microscopy probes the polarity distribution of collagen fibrils," Optica **7**, 1469–1476 (2020).
56. P. Schön, F. Munhoz, A. Gasecka, S. Brustlein, and S. Brasselet, "Polarization distortion effects in polarimetric two-photon microscopy," Opt. Express **16**, 20891–20901 (2008).
57. R. Kumar, K. M. Grønhaug, E. I. Romijn, A. Finnøy, C. L. Davies, J. O. Drogset, and M. B. Lilledahl, "Polarization second harmonic generation microscopy provides quantitative enhanced molecular specificity for tissue diagnostics," J. Biophoton. **8**, 730–739 (2015).
58. P.-J. Su, W.-L. Chen, T.-H. Li, C.-K. Chou, T.-H. Chen, Y.-Y. Ho, C.-H. Huang, S.-J. Chang, Y.-Y. Huang, and H.-S. Lee, "The discrimination of type I and type II collagen and the label-free imaging of engineered cartilage tissue," Biomaterials **31**, 9415–9421 (2010).
59. H. Mehidine, M. Sibai, F. Poulon, J. Pallud, P. Varlet, M. Zanello, B. Devaux, and D. Abi Haidar, "Multimodal imaging to explore endogenous fluorescence of fresh and fixed human healthy and tumor brain tissues," J. Biophoton. **12**, e201800178 (2019).
60. J. Trägårdh, "Polarization resolved SHG imaging through a multimode fiber," figshare, 2021, http://doi.org/10.6084/m9.figshare.14495070.